

pubs.acs.org/JACS Article

# Kinetically Controlled Synthesis of Rhodium Nanocrystals with Different Shapes and a Comparison Study of Their Thermal and Catalytic Properties

Ming Zhao, Sitao Chen, Yifeng Shi, Zachary D. Hood, Zhiheng Lyu, Minghao Xie, Miaofang Chi, and Younan Xia\*



Cite This: J. Am. Chem. Soc. 2021, 143, 6293-6302



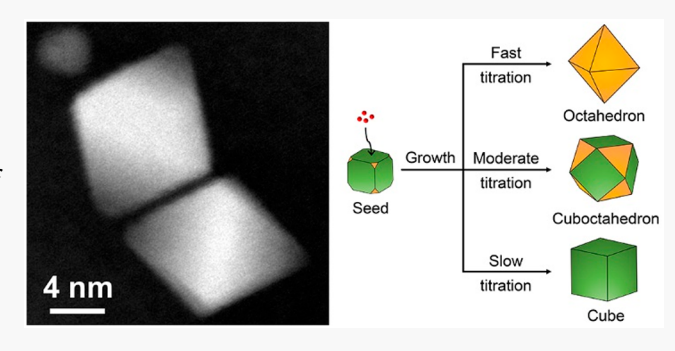
**ACCESS** 

Metrics & More

Article Recommendations

Supporting Information

ABSTRACT: We report the synthesis of Rh nanocrystals with different shapes by controlling the kinetics involved in the growth of preformed Rh cubic seeds. Specifically, Rh nanocrystals with cubic, cuboctahedral, and octahedral shapes can all be obtained from the same cubic seeds under suitable reduction kinetics for the precursor. The success of such a synthesis also relies on the use of a halide-free precursor to avoid oxidative etching, as well as the involvement of a sufficiently high temperature to remove Br<sup>-</sup> ions from the seeds while ensuring adequate surface diffusion. The availability of Rh nanocrystals with cubic and octahedral shapes allows for an evaluation of the facet dependences of their thermal and catalytic properties. The data from *in situ* electron microscopy



studies indicate that the cubic and octahedral Rh nanocrystals can keep their original shapes up to 700 and 500  $^{\circ}$ C, respectively. When tested as catalysts for hydrazine decomposition, the octahedral nanocrystals exhibit almost 4-fold enhancement in terms of  $H_2$  selectivity relative to the cubic counterpart. As for ethanol oxidation, the order is reversed, with the cubic nanocrystals being about three times more active than the octahedral sample.

# **■** INTRODUCTION

Colloidal metal nanocrystals with controlled shapes have found use in a wide variety of fundamental studies and applications. 1-5 In the context of catalysis, such nanocrystals provide well-defined surface structures for the establishment of structure-property relationship to guide the rational development of improved or new catalysts toward various reactions. 6-Specifically, it is a viable idea to optimize the catalytic activity and/or selectivity of nanocrystals toward a structure-sensitive reaction through shape-controlled synthesis. 10-13 This concept has been extensively explored using different systems, 14-17 but the simplest study should be based on a direct comparison of nanocrystals made of the same metal while taking cubic, cuboctahedral, and octahedral shapes to present the surface as a mix of  $\{100\}$  and  $\{111\}$  facets in different proportions. When made of Pt and evaluated as catalysts toward the oxygen reduction reaction in a perchlorate electrolyte, the octahedral nanocrystals were found to be five times more active than their cubic counterparts. 16 When tested as catalysts toward the hydrogenation of benzene, only cyclohexene was produced on nanocubes encased by {100} facets whereas both cyclohexane and cyclohexene were formed on cuboctahedral nanocrystals covered by a mix of {111} and {100} facets. These and many other examples demonstrate that the availability of metal nanocrystals featuring cubic, cuboctahedral, and octahedral

shapes would make it easy to examine the facet- or shape-dependence of a catalytic reaction.  $^{18-20}$ 

Thanks to the efforts from many research groups, now we can easily access nanocrystals with cubic, cuboctahedral, and octahedral shapes for a number of metals, including Ag, Au, Pd, and Pt.<sup>4,19,20</sup> In the case of Rh, despite the availability of well-established protocols for the synthesis of cubes, it is still challenging to produce cuboctahedral and octahedral nanocrystals in high quality and uniformity (Figure S1).<sup>21–24</sup> As a result, it has been difficult to investigate the structure–property relationship of Rh nanocrystals in terms of facet or shape dependence. The predicament can be understood from several aspects. First, the formation of Rh octahedral nanocrystals requires a fast reduction rate at the beginning for the generation of single-crystal seeds and then switching to a slow reduction rate for the expression of {111} facets favored by thermodynamics. For a one-pot synthesis involving

Received: March 12, 2021 Published: April 14, 2021





homogeneous nucleation, it is nontrivial to independently adjust the reduction kinetics for the nucleation and growth steps. <sup>25,26</sup> Second, the halide ions, either used as an additive or derived from the precursor, are detrimental to the formation of Rh nanocrystals uniform in size and shape. <sup>27–30</sup> The halide ions can combine with O<sub>2</sub> from air to cause oxidative etching during the nucleation and growth steps, resulting in the production of polydispersed samples. <sup>27,28</sup> The strong binding of halide ions to a specific type of facet, for example, Br<sup>-</sup> ions for the Rh{100} facets, tends to make the capped facets more favorable for expression in the final product. <sup>29,30</sup> Third, the bond energy of Rh–Rh (285 kJ mol<sup>-1</sup>) is much greater than those of Pd (100 kJ mol<sup>-1</sup>) and Ag (160 kJ mol<sup>-1</sup>), <sup>31</sup> creating a higher energy barrier to the diffusion of Rh adatoms and thus impeding the formation of a smooth surface.

In addressing these issues, we switched to seed-mediated growth and further demonstrated the synthesis of Rh nanocrystals with different shapes, including octahedra, cuboctahedra, and cubes. The success of such a synthesis critically relied on the manipulation of reduction kinetics through the use of a programmable syringe pump or a polyol with proper reduction power. To avoid possible oxidative etching and surface capping commonly associated with halide ions, it was necessary to use a halide-free Rh(III) precursor such as Rh(acac)<sub>3</sub>. Typically, the synthesis was conducted at 220 °C to help remove the Br ions adsorbed on the preformed cubic seeds while ensuring adequate surface diffusion for the formation of a smooth surface. By a simple increase in the volume of the reaction solution, the protocol based on triethylene glycol (TEG) and syringe pump allowed us to produce Rh octahedral nanocrystals of 8.9  $\pm$  0.8 nm in edge length at a scale of roughly 5 mg per batch. By replacing TEG with tetraethylene glycol (TTEG) and adding an adequate amount of poly(vinylpyrrolidone) (PVP) into the reaction mixture to tune the reaction kinetics, we also demonstrated the synthesis of Rh octahedra in the one-shot setting. A mechanistic study was further conducted to elucidate the impacts of TTEG and PVP on the reduction kinetics of the Rh(III) precursor. Such a one-pot synthesis can be potentially conducted in a continuous-flow reactor for scalable production. The as-obtained Rh nanocubes and octahedra allowed us to systematically evaluate the shape-dependent thermal and catalytic properties of Rh nanocrystals.

## EXPERIMENTAL SECTION

Chemicals and Materials. Rhodium(III) acetylacetonate (Rh-(acac)3, 97%) was obtained from Acros Organics. Ethylene glycol (EG, 99%) was purchased from J. T. Baker. Sodium hexachlororhodate(III) (Na<sub>3</sub>RhCl<sub>6</sub>, 97%), rhodium(III) chloride hydrate (RhCl<sub>3</sub>·xH<sub>2</sub>O, 99.98%), PVP (MW ≈ 55,000), perchloric acid (HClO<sub>4</sub>, 70%, PPT grade, Veritas), L-ascorbic acid (AA, 99%), potassium bromide (KBr, 99%), potassium hydroxide (KOH), TEG (99%), TTEG (99%), and hydrazine monohydrate (N<sub>2</sub>H<sub>4</sub>·H<sub>2</sub>O, 98%) were all purchased from Sigma-Aldrich. Ethanol (C2H5OH, anhydrous) was obtained from KOPTEC. Syringes and syringe pump were purchased from KD Scientific. Polyvinyl chloride tubing and capillaries were purchased from Thermo Scientific. The temperatures of all syntheses were monitored using a thermal sensor purchased from ACE Glass. Aqueous solutions were prepared using deionized (DI) water featuring a resistivity of 18.2 M $\Omega$  cm at room temperature.

**Synthesis of 4.5 nm Rh Cubic Seeds.** Typically, 13 mL of an EG solution containing AA (52.8 mg), KBr (108 mg), and PVP (133 mg) was transferred into a three-neck flask and heated at 140 °C under magnetic stirring (380 rpm) for 1 h. Meanwhile, 6 mL of

another EG solution containing 46.2 mg of  $Na_3RhCl_6$  was added into the flask at  $60 \text{ mL h}^{-1}$  for the first  $1.1 \text{ and } 4 \text{ mL h}^{-1}$  for the remaining 4.9 mL, respectively. After 3 h, the solid products were collected by centrifugation, washed once with acetone and three times with a mixture of ethanol and acetone.

**Synthesis of Rh Octahedral Nanocrystals.** In the standard protocol, 0.2 mg of the as-prepared 4.5 nm Rh cubes and 25 mg of PVP were mixed in 2 mL of TEG. The mixture was then transferred into a 20 mL vial and heated at 220 °C for 10 min under magnetic stirring (380 rpm). Meanwhile, 2.4 mL of a TEG solution containing Rh(acac) $_3$  (1 mg mL $^{-1}$ ) was added into the growth solution at a rate of 5 mL h $^{-1}$ . After all the precursor had been added, the reaction was continued for 1.5 h before quenching in an ice—water bath. The solid products were collected by centrifugation and washed once with acetone and three times with a mixture of ethanol and acetone. Figure S2 shows a schematic illustration of the setup used for the synthesis.

Scaling Up the Synthesis of Rh Octahedral Nanocrystals by Five Times. In a typical synthesis, 1 mg of the 4.5 nm Rh cubes, 125 mg of PVP, and 10 mL of TEG were mixed in a three-necked flask. The flask was then placed in an oil bath and heated to 220 °C under magnetic stirring (800 rpm). After 10 min, 12 mL of a TEG solution containing Rh(acac)<sub>3</sub> (1 mg mL<sup>-1</sup>) was dropwise added into the flask at a rate of 25 mL h<sup>-1</sup>. The reaction was allowed to continue for 1.5 h, after all the precursor had been added, and then quenched in an ice—water bath. The solid products were collected by centrifugation and washed once with acetone and three times with a mixture of ethanol and acetone.

Synthesis of Rh Octahedral Nanocrystals by Adding the Rh(III) Precursor in One Shot. Typically, 0.2 mg of the 4.5 nm Rh cubes, 1000 mg of PVP, and 2 mL of TTEG were mixed in a 20 mL vial and heated at 220 °C for 10 min under magnetic stirring (380 rpm). Meanwhile, 2.4 mL of a TTEG solution containing Rh(acac) $_3$  (1 mg mL $^{-1}$ ) was added into the growth solution in one shot. After 3 h, the solid products were collected by centrifugation and washed once with acetone and three times with a mixture of ethanol and acetone.

Characterizations. TEM images were taken on a Hitachi 7700 microscope. High-angle annular dark-field (HAADF) and bright-field (BF) scanning transmission electron microscopy (STEM) images were acquired on a Cs-corrected FEI Titan 80/300 kV microscope at Oak Ridge National Laboratory (ORNL). X-ray diffraction (XRD) patterns were recorded using a PANalytical X'Pert PRO Alpha-1 diffractometer using a 1.8 kW Ceramic Copper tube source. An inductively coupled plasma mass spectrometer (ICP-MS, NexION 300Q, PerkinElmer) was used to quantify the metal contents. The X-ray photoelectron spectroscopy (XPS) data were recorded on a Thermo K-Alpha spectrometer with an Al K $\alpha$  source.

Quantitative Ánalysis of Reduction Kinetics. In a typical study, 0.1 mL was sampled from the reaction solution every 10 min during a synthesis. The aliquot was then mixed with 0.9 mL of acetone to precipitate out all the particles, followed by centrifugation to leave behind the unreacted Rh(III) ions in the supernatant. The supernatant was then collected and diluted for ICP-MS analysis.

**Evaluation of Thermal Stability.** The thermal stability of the Rh nanocrystals was evaluated using *in situ* HRTEM coupled with a Protochips Aduro heating holder. Typically, an aqueous suspension of the as-prepared Rh nanocrystals was drop-cast onto the Aduro thermal device prior to drying under ambient conditions. The sample was then heated to various temperatures up to 800 °C at an interval of 100 °C. The heating rate was 1000 °C ms<sup>-1</sup>, and the sample was held at each specified temperature for 1 h.

**Hydrazine Decomposition Experiments.** In a typical measurement, 0.2 mg of the Rh catalyst was added into a two-necked flask, with one opening connected to a gas buret. Afterward,  $10~\mu L$  of  $N_2H_4$ · $H_2O$  was injected into the flask under magnetic stirring at room temperature. The volume of the produced gases was monitored using the gas buret after passing through 1.0 M HCl solution to ensure the complete removal of ammonia.

**Electrochemical Measurements.** The electrochemical measurements were conducted in a three-electrode cell using an electro-

chemical workstation (CHI 600E potentiostat). A Pt mesh and reversible hydrogen electrode (RHE) were used as the counter and reference electrodes, respectively. The as-synthesized Rh nanocrystals were loaded on a carbon support (Ketjenblack EC-300J, AkzoNobel) with a weight percentage of ca. 20 wt % and then used as the working electrode. Cyclic voltammograms (CVs) were recorded in a N2-saturated 0.1 M HClO4 solution, in the potential range of 0.08–1.1 V and at a scanning rate of 50 mV s<sup>-1</sup>. The linear sweep voltammograms (LSVs) were measured in a mixture of 1.0 M ethanol and 1.0 M KOH aqueous solutions, in the potential range of 0.08–1.2 V and at a scanning rate of 50 mV s<sup>-1</sup>. The potentials involved in this work were derived from E(RHE) and presented as E(SCE), where SCE denotes the saturated calomel electrode, according to the formula E(RHE) = E(SCE) + 0.2412 + 0.05916xpH.

## RESULTS AND DISCUSSION

Synthesis and Characterization of Rh Octahedral Nanocrystals. The synthesis started with the preparation of Rh nanocubes with an average edge length of  $4.5 \pm 0.4$  nm (Figure S3). The as-obtained nanocubes were then mixed with PVP in TEG held at 220 °C, followed by the dropwise addition of Rh(acac)<sub>3</sub> precursor solution to initiate heterogeneous nucleation and then growth. Figure 1a-d shows TEM images of the Rh nanocrystals obtained after the addition of 0.5, 1.0, 2.0, and 2.4 mL of the Rh(acac)<sub>3</sub> solution, indicating gradual evolution from cubes to truncated cubes, cuboctahedra, truncated octahedra, and octahedra, respectively. All these nanocrystals were enclosed by a mix of  $\{111\}$  and  $\{100\}$  facets,

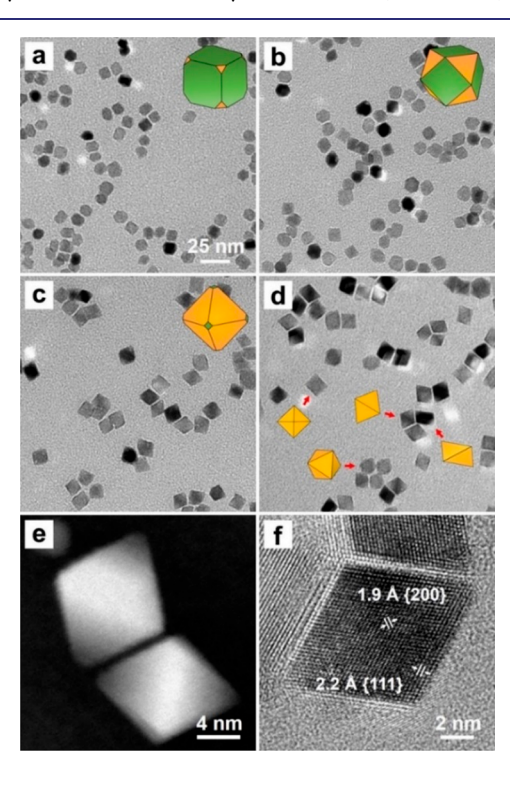


**Figure 1.** TEM images of the Rh nanocrystals prepared using the standard protocol except that different volumes of the Rh(acac)<sub>3</sub> solution were added into the reaction solution: (a) 0.5, (b) 1.0, (c) 2.0, and (d) 2.4 mL. The scale bar in panel a also applies to panels b—d. The insets in panels a—c indicate the shape taken by nanocrystals in each sample while those in panel d show models of an octahedron at different orientations. The green and yellow colors represent {100} and {111} facets, respectively. (e) HAADF-STEM image of two Rh octahedra. (f) Atomic-resolution STEM image recorded from one Rh octahedron.

and the ratio between their areas kept increasing as the volume of the  $Rh(acac)_3$  solution was increased. Eventually, Rh octahedral nanocrystals encased by  $\{111\}$  facets were obtained, and the average edge length was increased to  $9.0 \pm 0.8$  nm (Figure 1d). Figure 1e shows a HAADF-STEM image of two such octahedral nanocrystals. Figure 1f shows an atomic-resolution ABF-STEM image of an individual octahedral nanocrystal, where the lattice fringe spacing of 1.9 and 2.2 Å could be indexed to the  $\{200\}$  and  $\{111\}$  planes, respectively, of face-centered cubic (fcc) Rh. Figure S4 shows an XRD pattern of the as-synthesized Rh octahedral nanocrystals, further confirming the fcc phase.

Mechanistic Understanding of the Synthesis. During the synthesis of Rh octahedral nanocrystals via seed-mediated growth, the injection rate of the Rh(acac), precursor and thus the deposition rate of Rh atoms had to be carefully controlled in order to avoid homogeneous nucleation while ensuring heterogeneous nucleation and continuous growth on the seeds. To this end, we varied the injection rate of the precursor to examine its impact on the formation of Rh octahedral nanocrystals, as illustrated in Figure 2a-d. When the precursor was added in one shot instead of dropwise addition, the products contained a mix of icosahedra, nanoplates, and irregular nanoparticles, in addition to the desired octahedra. The byproducts were indicative of homogeneous nucleation, primarily due to the high concentration of Rh atoms caused by the one-shot injection of the precursor (Figure 2a). When we added the precursor at a rate of 30 mL h<sup>-1</sup>, the proportions of twinned and irregular nanoparticles decreased whereas Rh octahedra prevailed in the products (Figure 2b). As the pumping rate was reduced to 1 mL  $\check{h}^{-1}$ , cuboctahedral nanocrystals enclosed by a mix of {111} and {100} facets were obtained as the main product (Figure 2c). If we further reduced the pumping rate to 0.5 mL h<sup>-1</sup>, the resultant Rh nanocrystals took the same cubic shape as that of the seeds, showing well-defined {100} facets and an enlarged size of 9.1 ± 1.1 nm in terms of edge length (Figure 2d).

It should be pointed out that during the synthesis of 4.5 nm Rh cubic seeds, Br ions were used as a capping agent for the preferential expression of {100} facets on the surface. After the washing process, the surface of the cubic seeds should still be covered by some Br ions because of the strong binding strength involved. Figure S5 shows a Br 3d XPS spectrum of the Rh cubic seeds, in which the peak located at around 69 eV confirms the presence of residual Br ions. Due to the involvement of a temperature as high as 220 °C, the adsorbed Br ions were expected to desorb from the surface during the synthesis. As verified by the XPS result (Figure S5), the peak associated with Br ions essentially disappeared after the seeds had been heated at 220 °C for 2 h. Considering the extremely small amount of residual Br ions (at a level of nano mole for a full coverage on all the Rh seeds involved) and the desorption of most Br ions from the surface at 220 °C, the Br ions should not be able to exert a remarkable capping or etching effect on the growth process. This argument was validated by the formation of well-defined {111} facets on the Rh octahedral nanocrystals (Figure 1d-f). Figure S6 compares Br 3d XPS spectra of the Rh cubic, cuboctahedral, and octahedral nanocrystals (Figures 1d, and 2c,d) prepared from the 4.5 nm Rh cubes, confirming the absence of Br ions in these samples.

Figure 2e shows a schematic illustration of the mechanism underlying the formation of Rh polyhedral nanocrystals with

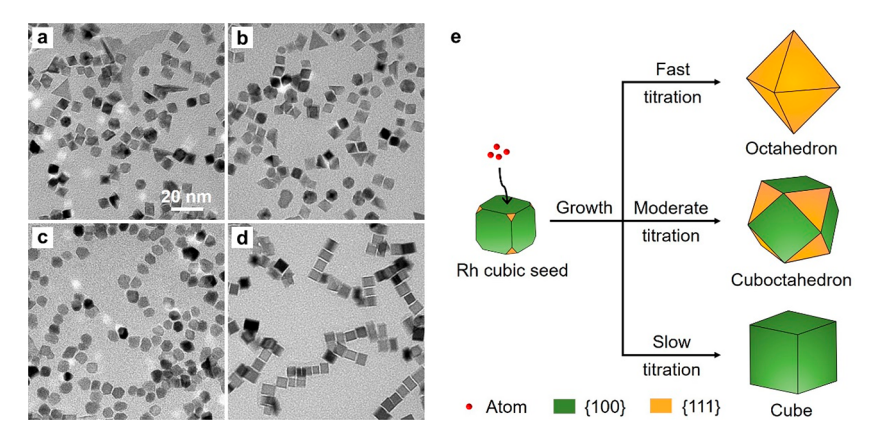


Figure 2. TEM images of the Rh nanocrystals prepared using the standard protocol except that the Rh(acac)<sub>3</sub> solution was added (a) in one shot and (b-d) at different pumping rates: (b) 30, (c) 1, and (d) 0.5 mL h<sup>-1</sup>. The scale bar in panel a applies to all panels b-d. (e) Schematic illustration showing the formation of various types of Rh polyhedral nanocrystals at different pumping rates for the precursor while keeping all other parameters the same as those in the standard synthesis.

diverse shapes at different pumping rates for the precursor in the case of heterogeneous nucleation only. Given the absence of capping agent and thus the accessibility of the entire surface for atom deposition, the newly generated atoms would be preferentially deposited on the side faces of the seeds relative to the corners owing to the higher surface energy of {100} facets than that of {111} facets. 34,35 When the pumping rate of the precursor was relatively fast (i.e., 5 mL h<sup>-1</sup>), the atoms would pile up on the {100} facets in the form of pyramids for the generation of  $\{111\}$  facets with a lower surface energy than that of {100} facets, giving rise to an octahedral shape. If the precursor was added at a moderate rate of 1 mL h<sup>-1</sup>, an increased number of the adatoms were able to diffuse to the corners and edges, resulting in the formation of cuboctahedral nanocrystals. This argument was further confirmed when a slow pumping rate of 0.5 mL h<sup>-1</sup> was involved. In this case, a large portion of the deposited Rh atoms would have sufficient time to diffuse across the entire surface and thereby replicate the cubic shape of the underlying seeds. Taken together, by varying the pumping rate of the Rh(acac)<sub>3</sub> precursor, we were able to control the growth pattern of Rh atoms in an kinetic manner and attain nanocrystals with a variety of shapes including octahedra, cuboctahedra, and cubes.

The reaction temperature is another parameter crucial to nanoparticles synthesis which affects both the reduction kinetics (i.e., deposition rate) of the metal precursor and surface diffusion kinetics of adatoms. In the content of generating well-defined Rh octahedral nanocrystals, an appropriate temperature should be leveraged not only to generate a proper number of atoms for continuous heterogeneous growth but also to ensure the preferential surface diffusion over atom deposition for the formation of a smooth surface. Figure S7 shows TEM images of the Rh nanocrystals prepared using the standard protocol except for the variation in reaction temperature. When the temperature was set to 160 °C, the resultant Rh nanocrystals took a cubic shape, with a size similar to that of the original cubic seeds (Figure S7a). This result could be attributed to the slow reduction kinetics of the precursor at such a low temperature, resulting in limited growth. If the temperature was elevated to 180 °C, the products showed obvious growth but took a rough surface owing to the lack of adequate surface diffusion (Figure S7b). When the temperature was further increased to 200 °C, truncated octahedral nanocrystals were obtained as the

prevalent products and their surface became smoother relative to those obtained at 180 °C (Figure S7c). If the synthesis was conducted at 240 °C, although surface diffusion was greatly enhanced, the generation of Rh atoms was also accelerated substantially, giving rise to the formation of diverse Rh nanocrystals through homogeneous nucleation (Figure S7d). It is worth noting that for Ag and Pd octahedra synthesized via seed-mediated growth, a smooth surface could be achieved at room temperature and 60 °C, respectively, whereas the expression of well-defined {111} surface for Rh octahedra required a reaction temperature as high as 220 °C. <sup>36,37</sup> The sharp contrast emphasizes the importance to optimize the reaction temperature in overcoming the high diffusion energy barrier of Rh atoms for the formation of a smooth surface. <sup>31</sup>

According to our prior work, oxidative etching enabled by the halide ions from the Rh precursor could greatly affect the shape of the final products.<sup>38,39</sup> Here, we also utilized different types of Rh precursors to examine their effect on the synthesis of Rh octahedra. Figure S8a,b shows TEM images of the Rh nanocrystals prepared using the standard protocol except for the involvement of Na<sub>3</sub>RhCl<sub>6</sub> and RhCl<sub>3</sub> as precursors, respectively. Compared with the standard sample shown in Figure 1d, there existed a large number of irregular nanoparticles and octahedral nanocrystals with a bumpy surface in both samples (as indicated by the arrows in Figure S8). This observation could be rationalized by the oxidative etching enabled by the Cl<sup>-</sup> ions from the precursors.<sup>38,39</sup> During the synthesis, the Cl<sup>-</sup> ions from Na<sub>3</sub>RhCl<sub>6</sub> or RhCl<sub>3</sub> served as a coordination ligand and the O2 from air served as an oxidant, forming an etchant for the Rh nanocrystals. In the etching process, the surface of the Rh nanocrystal acted as a cathode for the reduction of oxygen, while the Cl<sup>-</sup> ions served as a charge carrier and coordination ligand for the anodic oxidation and dissolution of metal atoms. 38,39 The involvement of oxidative etching could significantly affect the growth pattern of Rh atoms on the seeds, resulting in deviations from the well-defined octahedral shape. Additionally, because the molar ratio of Cl<sup>-</sup> to Rh<sup>3+</sup> in Na<sub>3</sub>RhCl<sub>6</sub> was two times greater than that in RhCl<sub>3</sub> (6:1 vs 3:1), oxidative etching was more significant for the resultant Rh nanocrystals prepared using Na<sub>3</sub>RhCl<sub>6</sub> as the precursor, further confirming the role of Cl<sup>-</sup> ions in oxidative etching (Figure S8a). This result is also consistent with the studies reported in literature, in which the involvement of RhCl<sub>3</sub> as the precursor would produce

nanocrystals that were notably deviated from well-defined octahedra (Figure S1).<sup>21,22</sup> Altogether, in order to prevent the occurrence of oxidative etching during the synthesis, a halidefree Rh precursor such as Rh(acac)<sub>3</sub> should be employed to attain Rh octahedral nanocrystals in high quality and with a smooth surface.

The use of preformed seeds was also essential to the synthesis of Rh octahedral nanocrystals. 40,41 The presence of monodispersed cubic seeds is advantageous not only in avoiding the potential heterogeneity arising from the homogeneous nucleation process but also in ensuring an identical growth behavior for each seed, giving rise to the formation of products in high quality and uniformity. In sharp contrast, if the standard synthesis was conducted in the absence of seeds, the products contained a mix of nanoplates, decahedra, icosahedra, and irregular nanoparticles (Figure S9), confirming the vital role of Rh seeds in directing the evolution of the octahedral shape. Additionally, the size of the seeds also played a critical role in controlling the formation of Rh octahedral nanocrystals because it determined the distance that the deposited Rh atoms would need to diffuse in order to generate a smooth surface. In general, small seeds are better suited for the adatoms to cover the entire surface by diffusion while large ones impose a long distance for the adatoms to diffuse across. Figure S10a shows the product prepared using the standard protocol except for the involvement of 9 nm Rh cubic seeds (Figure 2d). The resultant nanocrystals took irregular shapes and a rough surface, indicative of inadequate surface diffusion. When we decreased the pumping rate of the precursor to 0.5 mL h<sup>-1</sup>, Rh cubes with a concave surface were obtained (Figure S10b). At such a slow pumping rate, the diffusion of deposited atoms would be enhanced to form a smoother surface relative to the sample shown in Figure S10a, but still insufficient to drive the adatoms deposited on the edges or boundaries to diffuse across the large side faces, leading to the generation of a concave structure.

Scale-Up the Synthesis of Rh Octahedral Nanocrystals. Despite the success in the shape-controlled synthesis of noble-metal nanocrystals, it remains a grand challenge to bridge the gap between academic studies and industrial applications owing to the inability to produce the nanocrystals at a large scale while maintaining the tight control over their shapes. To mitigate this issue, we attempted to scale our synthesis up to five times by proportionally increasing the volumes of reaction solutions. Noticeably, the pumping rate of the precursor was also increased by five times to 25 mL h<sup>-1</sup> in order to generate adequate Rh atoms for the continuous growth on the seeds. Simultaneously, the reaction solution was magnetically stirred at an increased speed of 800 rpm to ensure the uniform dispersal of the injected precursor while avoiding local supersaturation of free Rh atoms for the initiation of homogeneous nucleation. Figure S11a shows a TEM image of the Rh nanocrystals synthesized using the scale-up protocol and they featured a well-defined octahedral shape and a uniform size distribution. According to the histogram of size distribution shown in Figure S11b, the average size of the resultant Rh octahedral nanocrystals was 8.9 ± 0.8 nm in edge length, consistent with that of the product from a standard

One-Shot Synthesis of Rh Octahedral Nanocrystals and the Kinetic Study. For the synthesis of Rh octahedral nanocrystals based upon seed-mediated growth, it was critical to manipulate the growth kinetics by dropwise adding the

Rh(acac)<sub>3</sub> solution at an appropriate rate using a programmable syringe pump. We also attempted to develop a one-shot method for the synthesis of Rh octahedra by optimizing the reagents to achieve the appropriate kinetic condition. Compared with the synthesis involving dropwise addition of the precursor solution, one-shot synthesis has additional benefits for easy operation and mechanistic study as well as potentials in a continuous-flow reactor for scaleup production. The one-shot synthesis was realized by switching from TEG to TTEG, as the solvent and reductant, and introducing a large amount of PVP into the synthesis, both of which have been demonstrated to decelerate the reduction kinetics of metal precursors through weakening the reducing capability and enhancing the steric hindrance, respectively. Figure 3a

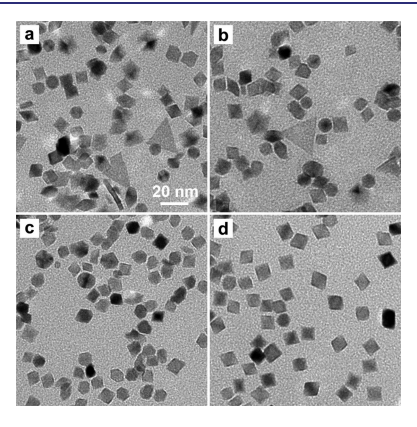


**Figure 3.** TEM images of the Rh nanocrystals prepared by adding the  $Rh(acac)_3$  solution into the TTEG solution in one shot, together with the use of PVP at different amounts: (a) 25, (b) 100, (c) 300, and (d) 1000 mg. The scale bar in panel a also applies to panels b–d.

shows a TEM image of the Rh nanocrystals prepared using the standard protocol except for the involvement of TTEG and the addition of the Rh(acac) $_3$  solution in one shot. The products contained icosahedra, nanoplates, and irregular nanocrystals, in addition to a small portion of octahedra. When the amount of PVP was increased to 100 mg and further to 300 mg, the proportion of twinned nanocrystals decreased whereas octahedral nanocrystals prevailed in the products (panels b and c of Figure 3, respectively). When 1000 mg of PVP was added into the synthesis, the products were dominated by Rh octahedral nanocrystals with well-defined {111} facets and an average size of 8.9  $\pm$  0.9 nm (Figure 3d), almost identical to the standard sample shown in Figure 1d.

To achieve a quantitative understanding of the mechanism involved in the one-shot synthesis of Rh octahedra, we conducted a kinetic study on the reduction of Rh(III) ions under different reaction conditions. Figure 4a shows the normalized concentrations of Rh(acac)<sub>3</sub> remaining in the solution during different syntheses, and they all decreased as a function of reaction time. Despite the same trend, the instantaneous concentrations of Rh(acac), differed remarkably from each other. When the one-shot synthesis was conducted in TEG, 90% of the precursor was depleted within 0.5 h. In comparison, only 64% of the precursor was consumed in 0.5 h when switching from TEG to TTEG, verifying the role of TTEG in decelerating the reduction kinetics of Rh(III) ions. As the amount of PVP was increased to 100, 300, and 1000 mg in the TTEG system, the conversion of the precursor in 0.5 h dropped to 54, 42, and 26%, respectively, suggesting that

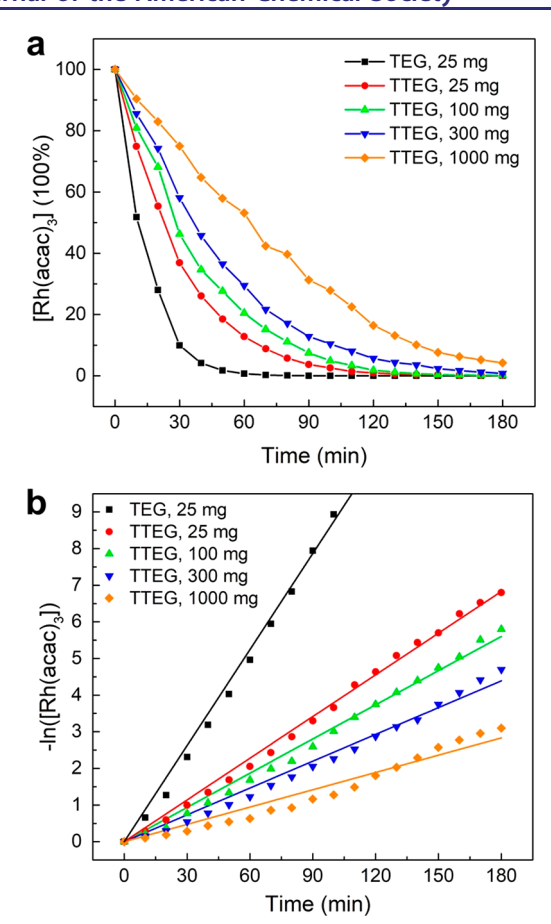


**Figure 4.** Quantitative analysis of the reduction kinetics of Rh(III) ions involved in the one-shot synthesis of Rh octahedra, where the type of polyol and the amount of PVP were varied. (a) Plots showing the normalized percentage of  $Rh(acac)_3$  remaining in the reaction solution as a function of reaction time. (b) Plots showing the linear relationship between  $-ln([Rh(acac)_3])$  and reaction time and the fitting based on the pseudo-first-order kinetics.

adding a larger amount of PVP could further retard the reduction kinetics of Rh(III) ions.

For the one-shot synthesis of Rh nanocrystals, the reduction of Rh(III) ions is expected to follow the second-order rate law due to the involvement of collision and electron transfer between the Rh(III) ions and reductant. 42 Given that the reductant (i.e., TEG or TTEG) was in great excess in the present study, its concentration could be assumed as unchanged during the synthesis. Therefore, the reaction rate could be fitted using the pseudo-first-order kinetics.<sup>41</sup> Figure 4b shows the linear dependence of  $-\ln([Rh(acac)_3])$  on the reaction time under different conditions, from which the rate constants were derived. By switching from TEG to TTEG while keeping other reaction conditions unchanged, the rate constant exhibited a 2.3-times drop from  $8.8 \times 10^{-2}$  to  $3.8 \times 10^{-2}$ 10<sup>-2</sup> min<sup>-1</sup>. When the amount of PVP was increased to 100, 300, and 1000 mg, the rate constant further decreased to 3.1  $\times$  $10^{-2}$ , 2.4 ×  $10^{-2}$ , and 1.5 ×  $10^{-2}$  min<sup>-1</sup>, respectively. Collectively, by replacing TEG with TTEG and adding 1000 mg of PVP into the reaction solution, we were able to decrease the reduction rate constant of Rh(III) ions by 5.9 times relative to the standard synthesis. As such, the concentration of the newly formed Rh atoms could be kept at a level below the supersaturation for homogeneous nucleation but high enough

for heterogeneous nucleation and growth on the seeds, enabling one-shot synthesis of Rh octahedral nanocrystals.

**Evaluation of the Shape-Dependent Thermal Stability.** Rh nanocrystals are well-documented as effective heterogeneous catalysts for a myriad of catalytic processes including syngas production and exhaust treatment, <sup>44–46</sup> which are typically operated under elevated temperatures. To study the shape-dependent response to thermal stress, we subjected the Rh cubic and octahedral nanocrystals with a similar size of 9 nm to *in situ* heating using HRTEM. As shown in Figure 5,

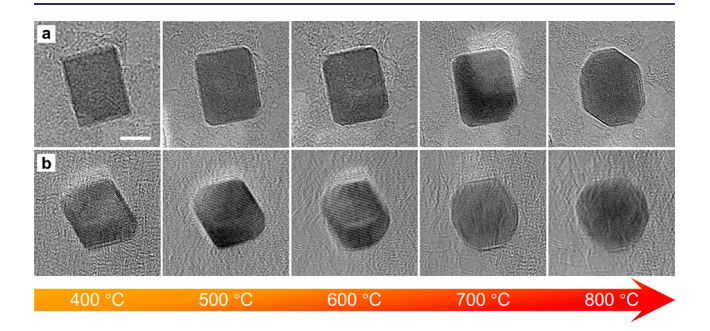


**Figure 5.** HRTEM images recorded from the same Rh (a) cube and (b) octahedron, respectively, when heated *in situ* to different temperatures in the range of 400-800 °C. The heating rate was 1000 °C ms<sup>-1</sup> and the nanocrystal was held at each marked temperature for 1 h before ramping to the next temperature. The scale bar is 5 nm and applies to all panels.

the original shapes of both the nanocrystals could be retained when heated up to 400 °C. However, as the temperature was further elevated, the two samples started to differ in terms of response. At 500 °C, the corners of the Rh cubic nanocrystal became slightly truncated while its side faces were still dominated by {100} facets (Figure 5a). The truncation became more significant as the temperature reached 700 °C. When the temperature reached 800 °C, the Rh cube evolved into a cuboctahedron, with its surface covered by a mix of {100} and {111} facets at roughly the same proportion (Figure 5a). With regard to the octahedral nanocrystal, its shape was largely maintained even after heating at 500 °C for 1 h, except for the minor rounding at the corners (Figure 5b). When the sample was heated to 600 °C, the nanocrystal showed major deviations from a well-defined octahedron and the {111} facets were greatly reduced in proportion. When the temperature was further elevated to 700 and then 800 °C, the particle eventually evolved into a spheroidal nanocrystal (Figure 5b). Taken together, the cubic and octahedral nanocrystals enclosed by {100} and {111} facets, respectively, could largely retain their original shapes up to 700 and 500 °C when subjected to heating under vacuum.

The superior thermal stability of cubic nanocrystals relative to the octahedral counterparts could be attributed to their different surface reconstruction behaviors.  $^{47-50}$  According to density functional theory (DFT) calculations, atoms on  $\{111\}$  facets typically preferred diffusion via hopping across the surface (i.e., the hopping mechanism) whereas those on the  $\{100\}$  facets tended to replace surface atoms by ejecting them to neighboring surface sites (i.e., the exchange mechanism).  $^{47-50}$  Since the energy barrier involved in the hopping process is lower than that in the exchange mechanism, the movement of adatoms on the  $\{111\}$  facets should be more facile than that on the  $\{100\}$  facets. In general, octahedral

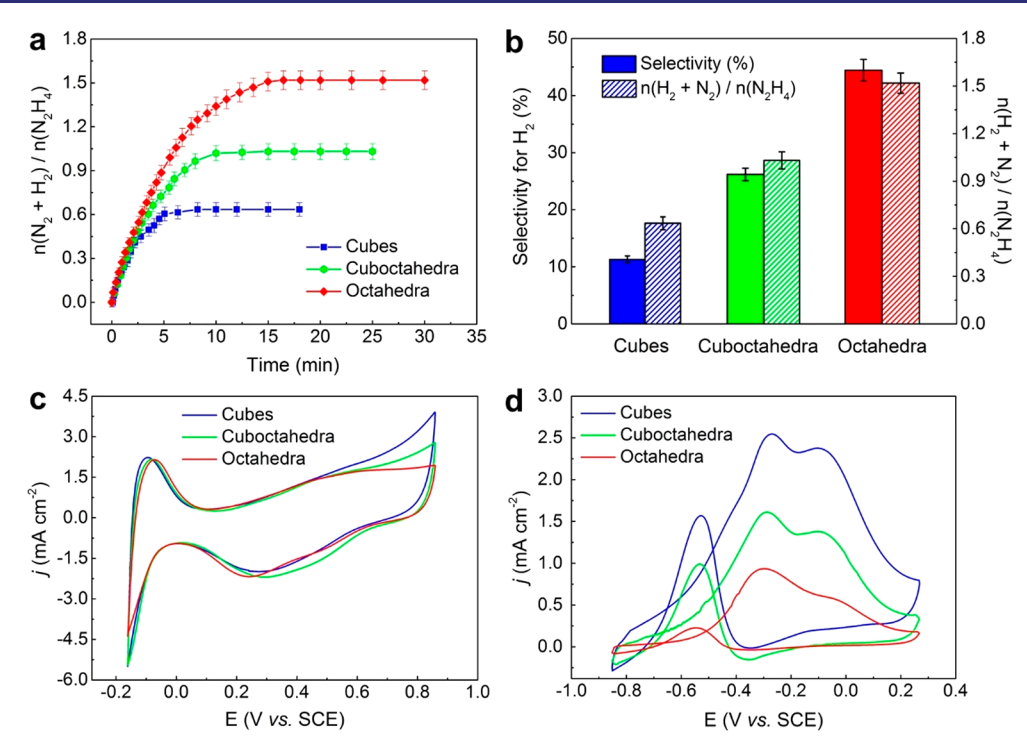


**Figure 6.** Comparison of the catalytic performance of Rh cubes, cuboctahedra, and octahedra toward hydrazine decomposition and ethanol oxidation. (a) Time-course plots for hydrazine decomposition in the presence of different types of Rh catalysts. (b) Selectivity for hydrogen generation from hydrazine decomposition catalyzed by different types of Rh nanocrystals. (c) CV curves measured for different types of Rh catalysts in a 0.1 M HClO<sub>4</sub> solution at a scanning rate of 50 mV s<sup>-1</sup>. (d) LSV curves of ethanol oxidation recorded in a mixture of 1.0 M ethanol and 1.0 M KOH solutions at a scanning rate of 50 mV s<sup>-1</sup>.

nanocrystals would be more vulnerable to thermal deformation than their cubic counterparts.

Evaluation of the Facet-Dependent Catalytic Performance. The catalytic performance of Rh nanocrystals has been proven to show strong shape dependence, whereas a study on Rh octahedral nanocrystals has not been accomplished due to the lack of Rh octahedra in high quality and uniformity. Here, we evaluated the facet-dependent performance of Rh nanocrystals in hydrazine decomposition by employing Rh nanocrystals with a similar size of 9 nm but covered by various shapes as the catalysts.<sup>50</sup> Figure 6a shows the plots for hydrazine decomposition in the presence of Rh cubes, cuboctahedra, and octahedra, which are enclosed by {100} facets, a mix of {100} and {111} facets, and {111} facets, respectively (Figures 1d, and 2c,d). The molar ratios of the generated H<sub>2</sub> and N<sub>2</sub> over the initially added hydrazine, denoted  $n(N_2 + H_2)/n(N_2H_4)$ , were derived as 0.6, 1.0, and 1.5 for the cubes, cuboctahedra, and octahedra, corresponding to H<sub>2</sub> selectivity of 11.3, 26.2, and 44.4%, respectively (Figure 6b). In particular, the Rh octahedra enclosed by {111} facets exhibited 3.9- and 1.7-fold enhancements in terms of H<sub>2</sub> selectivity relative to their cubic and cuboctahedral counterparts, respectively. The enhanced selectivity of Rh octahedra could be rationalized by the lower activation energy for the dehydrogenation of hydrazine molecules on Rh{111} facets relative to that on Rh{100} facets. 51-53 Additionally, the decreased transient Rh-H bond strength and adsorption affinity of intermediates on Rh{111} facets were also found to be advantageous in promoting H2 generation from hydrazine decomposition.51-53

We also assessed the catalytic activity of different Rh polyhedral nanocrystals toward the electrochemical oxidation

of ethanol. Figure 6c shows the CV curves recorded in an aqueous HClO4 solution over different Rh catalysts, from which the electrochemical surface areas (ECSAs) could be derived as 13.1, 18.0, and 17.2 m<sup>2</sup> g<sub>Rh</sub><sup>-1</sup> for Rh nanocrystals with cubic, cuboctahedral, and octahedral shapes, respectively. Figure 6d shows the ECSA-normalized LSV curves measured in a mixture of ethanol and KOH solutions. In the positivegoing curves, two characteristic oxidation peaks could be observed for different Rh catalysts, which were positioned at -0.3 and -0.1 V vs. SCE, respectively. The peak at -0.3 V could be attributed to the oxidation of ethanol to acetaldehyde and CO2, while the peak at -0.1 V corresponds to the involvement of acetic acid formation. 54,55 Additionally, the ECSA-normalized peak current density (i.e., specific activity) of Rh cubes was derived as 2.6 mA cm<sup>-2</sup>, which was 1.6 and 2.9 times as high as those of their cuboctahedral (1.6 mA cm<sup>-2</sup>) and octahedral (0.9 mA cm<sup>-2</sup>) counterparts, respectively. This result validated that the {100} facets on Rh nanocubes were more active than the {111} facets in catalyzing ethanol oxidation. The superior performance of Rh{100} facets is attributable to their higher surface free energy relative to Rh{111} facets, which was instrumental to promoting the C-C bond cleavage during the oxidation of ethanol molecules.<sup>54</sup> DFT calculations also suggested that compared with the closepacked {111} facets, the low-coordination atoms on the {100} facets exhibited a stronger binding strength and thus a lower energy barrier to both the dehydrogenation and C-C scission of ethanol molecules, leading to the boosted performance toward ethanol oxidation.<sup>54</sup>

# CONCLUSIONS

We have developed a robust protocol based on seed-mediated growth for the synthesis of Rh nanocrystals with three basic shapes of cubes, cuboctahedra, and octahedra. It was critical to exclude the etching and capping effects associated with halide ions by using Rh(acac)<sub>3</sub> as the precursor while ensuring adequate surface diffusion at a high enough temperature. In the case of TEG, it was also pivotal to add the precursor solution into a suspension of the cubic seeds with the use of a syringe pump to manipulate the reduction kinetics. With substituting TEG with TTEG while adding adequate PVP into the reaction solution to modulate the reduction kinetics, it was feasible to obtain Rh octahedra by directly adding the precursor solution in one shot. Our in situ electron microscopy studies indicate that the original shape of Rh nanocubes could be largely maintained up to 700 °C, 200 °C higher than their octahedral counterparts. When tested as catalysts for hydrazine decomposition, the {111} facets on Rh octahedral nanocrystals were found to be almost four times more selective toward H<sub>2</sub> production when benchmarked against the {100} facets on Rh nanocubes. As for ethanol oxidation, Rh nanocubes outperformed their octahedral counterparts by almost three times in terms of activity. Taken together, this work provides an effective strategy based on kinetic manipulation for the synthesis of Rh nanocrystals with diverse but controllable shapes, together with insights into their shape-dependent thermal and catalytic properties.

# ASSOCIATED CONTENT

# Supporting Information

The Supporting Information is available free of charge at https://pubs.acs.org/doi/10.1021/jacs.1c02734.

TEM images and XPS data of Rh cubic seeds and Rh nanocrystals prepared under different experimental conditions are provided. XRD pattern of the Rh octahedra prepared using the standard protocol is also included (PDF)

# AUTHOR INFORMATION

#### **Corresponding Author**

Younan Xia — School of Chemistry and Biochemistry and School of Chemical and Biomolecular Engineering, Georgia Institute of Technology, Atlanta, Georgia 30332, United States; The Wallace H. Coulter Department of Biomedical Engineering, Georgia Institute of Technology and Emory University, Atlanta, Georgia 30332, United States;

orcid.org/0000-0003-2431-7048; Email: younan.xia@bme.gatech.edu

# **Authors**

Ming Zhao – School of Chemistry and Biochemistry, Georgia Institute of Technology, Atlanta, Georgia 30332, United States; © orcid.org/0000-0003-0127-1470

Zitao Chen – The Wallace H. Coulter Department of Biomedical Engineering, Georgia Institute of Technology and Emory University, Atlanta, Georgia 30332, United States; orcid.org/0000-0002-6111-7750

Yifeng Shi — School of Chemical and Biomolecular Engineering, Georgia Institute of Technology, Atlanta, Georgia 30332, United States

Zachary D. Hood – School of Chemistry and Biochemistry, Georgia Institute of Technology, Atlanta, Georgia 30332, United States; Center for Nanophase Materials Sciences, Oak Ridge National Laboratory, Oak Ridge, Tennessee 37831, United States

Zhiheng Lyu — School of Chemistry and Biochemistry, Georgia Institute of Technology, Atlanta, Georgia 30332, United States; orcid.org/0000-0002-1343-4057

Minghao Xie — School of Chemistry and Biochemistry, Georgia Institute of Technology, Atlanta, Georgia 30332, United States; orcid.org/0000-0003-3781-5118

Miaofang Chi — Center for Nanophase Materials Sciences, Oak Ridge National Laboratory, Oak Ridge, Tennessee 37831, United States; Oorcid.org/0000-0003-0764-1567

Complete contact information is available at: https://pubs.acs.org/10.1021/jacs.1c02734

## **Author Contributions**

\*These authors contributed equally to this work.

#### **Notes**

The authors declare no competing financial interest.

# ACKNOWLEDGMENTS

This work was supported in part by a grant from NSF (CHE-1804970) and start-up funds from the Georgia Institute of Technology. Microscopy and XRD analyses were conducted at Institute of Electronics and Nanotechnology (IEN, Georgia Institute of Technology) supported by the NSF (ECCS-1542174). Part of the electron microscopy analyses was carried out in the Center for Nanophase Materials Sciences in ORNL, which is a DOE Office of Science User Facility (M.C. and Z.D.H.). Z.D.H. gratefully acknowledges support from the NSF Graduate Research Fellowship (DGE-1650044) and the Georgia Tech-ORNL Fellowship.

# ■ REFERENCES

- (1) Guntern, Y. T.; Okatenko, V.; Pankhurst, J.; Varandili, S. B.; Iyengar, P.; Koolen, C.; Stoian, D.; Vavra, J.; Buonsanti, R. Colloidal Nanocrystals as Electrocatalysts with Tunable Activity and Selectivity. *ACS Catal.* **2021**, *11*, 1248–1295.
- (2) You, H.; Yang, S.; Ding, B.; Yang, H. Synthesis of colloidal metal and metal alloy nanoparticles for electrochemical energy applications. *Chem. Soc. Rev.* **2013**, *42*, 2880–2904.
- (3) Xie, C.; Niu, Z.; Kim, D.; Li, M.; Yang, P. Surface and Interface Control in Nanoparticle Catalysis. *Chem. Rev.* **2020**, 120, 1184–1249.
- (4) Shi, Y.; Lyu, Z.; Zhao, M.; Chen, R.; Nguyen, Q. N.; Xia, Y. Noble-Metal Nanocrystals with Controlled Shapes for Catalytic and Electrocatalytic Applications. *Chem. Rev.* **2021**, *121*, 649–735.
- (5) Chen, Q.; Jia, Y.; Xie, S.; Xie, Z. Well-faceted noble-metal nanocrystals with nonconvex polyhedral shapes. *Chem. Soc. Rev.* **2016**, 45, 3207–3220.
- (6) Strasser, P.; Gliech, M.; Kuehl, S.; Moeller, T. Electrochemical process on solid shaped nanoparticles with defined facets. *Chem. Soc. Rev.* **2018**, *47*, 715–735.
- (7) Zhu, W.; Kattel, S.; Jiao, F.; Chen, J. G. Shape-Controlled  $\rm CO_2$  Electrochemical Reduction on Nanosized Pd Hydride Cubes and Octahedra. *Adv. Energy Mater.* **2019**, *9*, 1802840.
- (8) Lyu, Z.; Zhu, S.; Xu, L.; Chen, Z.; Zhang, Y.; Xie, M.; Li, T.; Zhou, S.; Liu, J.; Chi, M.; Shao, M.; Mavrikakis, M.; Xia, Y. Kinetically Controlled Synthesis of Pd—Cu Janus Nanocrystals with Enriched Surface Structures and Enhanced Catalytic Activities toward CO<sub>2</sub> Reduction. *J. Am. Chem. Soc.* **2021**, *143*, 149–162.
- (9) Collins, G.; Schmidt, M.; O'Dwyer, C.; Holmes, J. D.; McGlacken, G. P. The Origin of Shape Selectivity in Palladium-Catalyzed Suzuki-Miyaura Cross Coupling Reactions. *Angew. Chem., Int. Ed.* **2014**, 53, 4142–4145.

- (10) Li, Z.; Ji, S.; Liu, Y.; Cao, X.; Tian, S.; Chen, Y.; Niu, Z.; Li, Y. Well-Defined Materials for Heterogeneous Catalysis: From Nanoparticles to Isolated Single-Atom Sites. *Chem. Rev.* **2020**, *120*, 623–682.
- (11) Guo, S.; Zhang, S.; Sun, S. Tuning Nanoparticle Catalysis for the Oxygen Reduction Reaction. *Angew. Chem., Int. Ed.* **2013**, *52*, 8526–8544.
- (12) Watt, J.; Cheong, S.; Tilley, R. D. How to control the shape of metal nanostructures in organic solution phase synthesis for plasmonics and catalysis? *Nano Today* **2013**, *8*, 198–215.
- (13) Wu, Y.; Wang, D.; Li, Y. Nanocrystals from solutions: catalysts. Chem. Soc. Rev. 2014, 43, 2112–2124.
- (14) Wu, Y.; Cai, S.; Wang, D.; He, W.; Li, Y. Synthesis of Water-Soluble Octahedral, Truncated Octahedral, and Cubic Pt–Ni Nanocrystals and Their Structure-Activity Study in Model Hydrogenation Reactions. *J. Am. Chem. Soc.* **2012**, *134*, 8975–8981.
- (15) Yu, N.; Tian, N.; Zhou, Z.; Sheng, T.; Lin, W.; Ye, J.; Liu, S.; Ma, H.; Sun, S. Pd Nanocrystals with Continuously Tunable High-Index Facets as a Model Nanocatalyst. *ACS Catal.* **2019**, *9*, 3144–3152.
- (16) Lee, C.-T.; Yang, X.; Vara, M.; Gilroy, K. D.; Xia, Y. Water-Based Synthesis of Sub-10 nm Pt Octahedra and Their Performance towards the Oxygen Reduction Reaction. *ChemNanoMat* **2017**, 3, 879–884.
- (17) Bratile, K. M.; Lee, H.; Komvopoulos, K.; Yang, P.; Somorjai, G. A. Platinum Nanoparticle Shape Effects on Benzene Hydrogenation Selectivity. *Nano Lett.* **2007**, *7*, 3097–3101.
- (18) Xie, S.; Liu, X.; Xia, Y. Shape-controlled syntheses of rhodium nanocrystals for the enhancement of their catalytic properties. *Nano Res.* **2015**, *8*, 82–96.
- (19) Kang, Y.; Yang, P.; Markovic, N. M.; Stamenkovic, V. R. Shaping electrocatalysis through tailored nanomaterials. *Nano Today* **2016**, *11*, 587–600.
- (20) Wu, B.; Zheng, N. Surface and interface control of noble metal nanocrystals for catalytic and electrocatalytic applications. *Nano Today* **2013**, *8*, 168–197.
- (21) Biacchi, A. J.; Schaak, R. E. The Solvent Matters: Kinetic *versus* Thermodynamic Shape Control in the Polyol Synthesis of Rhodium Nanoparticles. *ACS Nano* **2011**, *5*, 8089–8099.
- (22) Long, N. V.; Chien, N. D.; Hirata, H.; Matsubara, T.; Ohtaki, M.; Nogami, M. Highly monodisperse cubic and octahedral rhodium nanocrystals: Their evolutions from sharp polyhedrons into branched nanostructures and surface-enhanced Raman scattering. *J. Cryst. Growth* **2011**, 320, 78–89.
- (23) Luo, L.; Li, H.; Peng, Y.; Feng, C.; Zeng, J. Rh-Based Nanocatalysts for Heterogeneous Reactions. *ChemNanoMat* **2018**, *4*, 451–466.
- (24) Zhang, Y.; Grass, M. E.; Kuhn, J. N.; Tao, F.; Habas, S. E.; Huang, W.; Yang, P.; Somorjai, G. A. Highly Selective Synthesis of Catalytically Active Monodisperse Rhodium Nanocubes. *J. Am. Chem. Soc.* **2008**, *130*, 5868–5869.
- (25) Zhang, H.; Li, W.; Jin, M.; Zeng, J.; Yu, T.; Yang, D.; Xia, Y. Controlling the Morphology of Rhodium Nanocrystals by Manipulating the Growth Kinetics with a Syringe Pump. *Nano Lett.* **2011**, *11*, 898–903.
- (26) Duan, H.; Yan, N.; Yu, R.; Chang, C.; Zhou, G.; Hu, H.; Rong, H.; Niu, Z.; Mao, J.; Asakura, H.; Tanaka, T.; Dyson, P. J.; Li, J.; Li, Y. Ultrathin rhodium nanosheets. *Nat. Commun.* **2014**, *5*, 3093.
- (27) Zhang, N.; Shao, Q.; Pi, Y.; Guo, J.; Huang, X. Solvent-Mediated Shape Tuning of Well-Defined Rhodium Nanocrystals for Efficient Electrochemical Water Splitting. *Chem. Mater.* **2017**, 29, 5009–5015.
- (28) Kuo, C.; Kao, C.; Chen, W.; Lu, Y.; Cullen, D. A.; Sneed, B. T.; Chuang, Y.; Yu, C.; Kuo, C. Aqueous Synthesis of Concave Rh Nanotetrahedra with Defect-Rich Surfaces: Insights into Growth-Defect-, and Plasmon-Enhanced Catalytic Energy Conversion. *Chem. Mater.* **2018**, *30*, 4448–4458.

- (29) Biacchi, A. J.; Schaak, R. E. Ligand-Induced Fate of Embryonic Species in the Shape-Controlled Synthesis of Rhodium Nanoparticles. *ACS Nano* **2015**, *9*, 1707–1720.
- (30) Ghosh, S.; Manna, L. The Many "Facets" of Halide Ions in the Chemistry of Colloidal Inorganic Nanocrystals. *Chem. Rev.* **2018**, *118*, 7804–7864.
- (31) Lide, D. CRC Handbook of Chemistry and Physics, 84th ed.; CRC Press: Boca Raton, FL, 2003; Vol. 9, pp 52-64.
- (32) Xie, S.; Lu, N.; Xie, Z.; Wang, J.; Kim, M. J.; Xia, Y. Synthesis of Pd–Rh Core–Frame Concave Nanocubes and Their Conversion to Rh Cubic Nanoframes by Selective Etching of the Pd Cores. *Angew. Chem., Int. Ed.* **2012**, *51*, 10266–10270.
- (33) Xie, S.; Peng, H.-C.; Lu, N.; Wang, J.; Kim, M. J.; Xie, Z.; Xia, Y. Confining the Nucleation and Overgrowth of Rh to the {111} Facets of Pd nanocrystal Seeds: The Roles of Capping Agent and Surface Diffusion. *J. Am. Chem. Soc.* **2013**, *135*, 16658–16667.
- (34) Sneed, B. T.; Brodsky, C. N.; Kuo, C.-H.; Lamontagne, L. K.; Jiang, Y.; Wang, Y.; Tao, F.; Huang, W.; Tsung, C.-K. Nanoscale-Phase-Separated Pd—Rh Boxes Synthesized *via* Metal Migration: An Archetype for Studying Lattice Strain and Composition Effects in Electrocatalysis. *J. Am. Chem. Soc.* **2013**, *135*, 14691–14700.
- (35) Xia, X.; Xie, S.; Liu, M.; Peng, H.; Lu, N.; Wang, J.; Kim, M. J.; Xia, Y. On the role of surface diffusion in determining the shape or morphology of noble-metal nanocrystals. *Proc. Natl. Acad. Sci. U. S. A.* **2013**, *110*, 6669–6673.
- (36) Jin, M.; Zhang, H.; Xie, Z.; Xia, Y. Palladium nanocrystals enclosed by {100} and {111} facets in controlled proportions and their catalytic activities for formic acid oxidation. *Energy Environ. Sci.* **2012**, *5*, 6352–6357.
- (37) Wang, Y.; Wan, D.; Xie, S.; Xia, X.; Huang, C.; Xia, Y. Synthesis of Silver Octahedra with Controlled Sizes and Optical Properties *via* Seed-Mediated Growth. *ACS Nano* **2013**, *7*, 4586–4594.
- (38) Zhang, H.; Xia, X.; Li, W.; Zeng, J.; Dai, Y.; Yang, D.; Xia, Y. Facile Synthesis of Five-fold Twinned, Starfish-like Rhodium Nanocrystals by Eliminating Oxidative Etching with a Chloride-Free Precursor. *Angew. Chem., Int. Ed.* **2010**, *49*, 5296–5300.
- (39) Long, R.; Zhou, S.; Wiley, B. J.; Xiong, Y. Oxidative etching for controlled synthesis of metal nanocrystals: atomic addition and subtraction. *Chem. Soc. Rev.* **2014**, *43*, 6288–6310.
- (40) Xia, Y.; Gilroy, K. D.; Peng, H.-C.; Xia, X. Seed-Mediated Growth of Colloidal Metal Nanocrystals. *Angew. Chem., Int. Ed.* **2017**, *56*, 60–95.
- (41) Niu, W.; Zhang, L.; Xu, G. Seed-mediated growth of noble metal nanocrystals: crystal growth and shape control. *Nanoscale* **2013**, 5, 3172–3181.
- (42) Wang, Y.; He, J.; Liu, C.; Chong, W. H.; Chen, H. Thermodynamics versus Kinetics in Nanosynthesis. Angew. Chem., Int. Ed. 2015, 54, 2022–2051.
- (43) Koczkur, K. M.; Mourdikoudis, S.; Polavarapu, L.; Skrabalak, S. E. Polyvinylpyrrolidone (PVP) in nanoparticle synthesis. *Dalton Trans.* **2015**, *44*, 17883–17905.
- (44) Kyriakou, V.; Neagu, D.; Zafeiropoulos, G.; Sharma, R. K.; Tang, C.; Kousi, K.; Metcalfe, I. S.; van de Sanden, M. C. M.; Tasmpas, M. N. Symmetrical Exsolution of Rh Nanoparticles in Solid Oxide Cells for Efficient Syngas Production from Greenhouse Gases. *ACS Catal.* **2020**, *10*, 1278–1288.
- (45) Lambert, C. K. Current state of the art and future needs for automotive exhaust catalysis. *Nat. Catal.* **2019**, *2*, 554–557.
- (46) Asakura, H.; Hosokawa, S.; Ina, T.; Kato, K.; Nitta, K.; Uera, K.; Uruga, T.; Miura, H.; Shishido, T.; Ohyama, J.; Satsuma, A.; Sato, K.; Yamamoto, A.; Hinokuma, S.; Yoshida, H.; Machida, M.; Yamazoe, S.; Tsukuda, T.; Teramura, K.; Tanaka, T. Dynamic Behavior of Rh Species in Rh/Al<sub>2</sub>O<sub>3</sub> Model Catalyst during Three-Way Catalytic Reaction: An Operando X-ray Absorption Spectroscopy Study. *J. Am. Chem. Soc.* **2018**, *140*, 176–184.
- (47) Zhao, M.; Chen, Z.; Lyu, Z.; Hood, Z. D.; Xie, M.; Vara, M.; Chi, M.; Xia, Y. Ru Octahedral Nanocrystals with a Face-Centered Cubic Structure, {111} Facets, Thermal Stability up to 400 °C, and Enhanced Catalytic Activity. *J. Am. Chem. Soc.* **2019**, *141*, 7028–7036.

- (48) Vara, M.; Roling, L. T.; Wang, X.; Elnabawy, A. O.; Hood, Z. D.; Chi, M.; Mavrikakis, M.; Xia, Y. Understanding the Thermal Stability of Palladium—Platinum Core—Shell Nanocrystals by *In Situ* Transmission Electron Microscopy and Density Functional Theory. *ACS Nano* **2017**, *11*, 4571–4581.
- (49) Chi, M.; Wang, C.; Lei, Y.; Wang, G.; Li, D.; More, K. L.; Lupini, A.; Allard, L. F.; Markovic, N. M.; Stamenkovic, V. R. Surface faceting and elemental diffusion behavior at atomic scale for alloy nanoparticles during *in situ* annealing. *Nat. Commun.* **2015**, *6*, 8925.
- (50) Singh, S. K.; Zhang, X.; Xu, Q. Room-Temperature Hydrogen Generation from Hydrous Hydrazine for Chemical Hydrogen Storage. *J. Am. Chem. Soc.* **2009**, *131*, 9894–9895.
- (51) Bai, J.; Xu, G.; Xing, S.; Zeng, J.; Jiang, J.; Chen, Y. Hydrothermal Synthesis and Catalytic Application of Ultrathin Rhodium Nanosheet Nanoassemblies. ACS Appl. Mater. Interfaces 2016, 8, 33635–33641.
- (52) Deng, Z.; Lu, X.; Wen, Z.; Wei, S.; Liu, Y.; Fu, D.; Zhao, L.; Guo, W. Mechanistic insight into the hydrazine decomposition on Rh(111): effect of reaction intermediate on catalytic activity. *Phys. Chem. Chem. Phys.* **2013**, *15*, 16172–16182.
- (53) Kang, Y.; Xue, Q.; Peng, R.; Jin, P.; Zeng, J.; Jiang, J.; Chen, Y. Bimetallic AuRh nanodendrites consisting of Au icosahedron cores and atomically ultrathin Rh nanoplate shells: synthesis and lightenhanced catalytic activity. NPG Asia Mater. 2017, 9, No. e407.
- (54) Zhang, J.; Ye, J.; Fan, Q.; Jiang, Y.; Zhu, Y.; Li, H.; Cao, Z.; Kuang, Q.; Cheng, J.; Zheng, J.; Xie, Z. Cyclic Penta-Twinned Rhodium Nanobranches as Superior Catalysts for Ethanol Electro-oxidation. J. Am. Chem. Soc. 2018, 140, 11232–11240.
- (55) Li, H.; Fan, Q.; Ye, J.; Cao, Z.; Ma, Z.; Jiang, Y.; Zhang, J.; Cheng, J.; Xie, Z.; Zheng, L. Excavated Rh nanobranches boost ethanol electro-oxidation. *Mater. Today Energy* **2019**, *11*, 120–127.